Islam et al, Ultrafine particle transport and deposition in a large scale 17-generation lung model., Journal of Biomechanics, 2017, 64 pp. 16 - 25

Ultrafine Particle Transport and Deposition in a Large Scale 17-Generation Lung Model

Mohammad S. Islam[a], Suvash C. Saha[1, a, *], Emilie Sauret[a], Tevfik Gemci[b], Ian A. Yang[c], Y.T. Gu[a]

[a]*School of Chemistry, Physics & Mechanical Engineering, Queensland University of Technology (QUT), 2 George Street, GPO Box 2434, Brisbane QLD 4001, Australia*

[b]*Validation Engineer Specialist, B. Braun Medical Inc., 2525 McGaw Avenue, Irvine, CA,USA*

[c] *Department of Thoracic Medicine, The Prince Charles Hospital, Metro North Hospital and Health Service, and Faculty of Medicine, The University of Queensland, Brisbane, Australia.*

**Corresponding author: Email: s_c_saha@yahoo.com, Tel:+61731381413*

Abstract:

To understand how to assess optimally the risks of inhaled particles on respiratory health, it is necessary to comprehend the uptake of ultrafine particulate matter by inhalation during the complex transport process through a non-dichotomously bifurcating network of conduit airways. It is evident that the highly toxic ultrafine particles damage the respiratory epithelium in the terminal bronchioles. The wide range of *in silico* available and the limited realistic model for the extrathoracic region of the lung have improved understanding of the ultrafine particle transport and deposition (TD) in the upper airways. However, comprehensive ultrafine particle TD data for the real and entire lung model are still unavailable in the literature. Therefore, this study is aimed to provide an understanding of the ultrafine particle TD in the terminal bronchioles for the

[1] Current address: School of Mechanical and Mechatronic Engineering, Faculty of Engineering and Information Technology, University of Technology Sydney, Ultimo NSW 2007, Australia

development of future therapeutics. The Euler-Lagrange (E-L) approach and ANSYS fluent (17.2) solver were used to investigate ultrafine particle TD. The physical conditions of sleeping, resting, and light activity were considered in this modelling study. A comprehensive pressure-drop along five selected path lines in different lobes was calculated. The non-linear behaviour of pressure-drops is observed, which could aid the health risk assessment system for patients with respiratory diseases. Numerical results also showed that ultrafine particle-deposition efficiency (DE) in different lobes is different for various physical activities. Moreover, the numerical results showed hot spots in various locations among the different lobes for different flow rates, which could be helpful for targeted therapeutical aerosol transport to terminal bronchioles and the alveolar region.

Keywords: Respiratory health risk assessment; ultrafine particle deposition; drug delivery; lobar deposition; pharmaceutical aerosol.

Introduction

Different natural sources (hot volcanic lava, smoke, ocean spray etc.) and also from traffic, home cooking, and complicated chemical reactions expose significant amount of ultrafine particles into the atmosphere. Moreover, the increased popularity of nanomaterial products and industrialization of nanomaterials may increase the emission of ultrafine particles (Lee *et al*., 2011) into the atmosphere. Inhaled nanoparticles deposit into extrathoracic airways result in strong diffusion and thermophoretic effects (Asgharian and Price, 2007). Due to their tiny size (d_p<1μm) (Zhang and Kleinstreuer, 2004), ultrafine particles can travel up to the alveoli. A certain percentage of those particles may deposit on the surface of the airways and interact with the epithelium, submucosa, and vessels of the airways (Gehr and Heyder, 2000; Rothen-Rutishauser *et al.*, 2005). These ultrafine particles may be soluble in the epithelium fluid, taken up by epithelium cells, or adhere

to the interstitium of the pulmonary airways (Gehr and Heyder, 2000). Depending upon the residence time and the toxicity, the deposited nanoparticles can result in various pulmonary diseases (Frampton, 2001; Gehr and Heyder, 2000). Evidence suggests that these nano-sized particles are actually more harmful to the respiratory system compare to the micro-size particles (Frampton, 2001; Oberdörster, 2000; Hsiao and Huang, 2013). The deposition of highly toxic ultrafine particles with bounded toxic carriers produces inflammation in the pulmonary epithelium, which is characterized by inflammatory cell infiltration and activation of vascular endothelial adhesion molecules (Laumbach and Kipen, 2012). The damaged epithelium cells ultimately reduce mucociliary clearance rate in the respiratory system and lead to various lung diseases (Diat-Sanchez, 1997). For this reason, a comprehensive investigation of ultrafine particle TD in a whole lung model, considering a possible entire branching pattern, is essential for a comprehensive health-risk assessment of potentially toxic particles.

A wide range of numerical studies has been conducted on ultrafine particles TD in the extrathoracic region, including the nasal and oral passages, the pharynx, and larynx (Cheng et al., 1996; Cheng et al., 1988; Inthavong et al., 2011; Shi et al., 2006; Swift et al., 1992; Xi and Longest, 2008a, b; Zhang and Kleinstreuer, 2011a). A computer simulation of the ultrafine particle diffusion pattern in a single bifurcation airway model was conducted by Yu *et al.* (1996). They concluded that the inlet condition significantly influences the flow and concentration distribution pattern. A comprehensive airflow structure and nanoparticles deposition study (Zhang and Kleinstreuer, 2004) for the first three generations (G0-G3) of the Weibel-based pulmonary model illustrates that the regional DE of a certain range ($1 \leq nm \leq 150$) of nanoparticles could be linked to the diffusion parameter. Local deposition of large nanoparticles (100 nm) is more uniformly dispersed than smaller (1 nm) nanoparticles (Zhang *et al.*, 2005). Longest and Xi (2007) showed the effect of

direct Lagrangian approach for ultrafine particle deposition in the upper airways by considering the finite inertia-and-slip correction factor. Farhadi Ghalati *et al.* (2012) found four major hot spots in a study of total and regional nanoparticle deposition fraction in a realistic CT-based model that reached to the trachea. Moskal and Gradoń (2002) investigated spatial deposition of aerosol nanoparticles for the first two generations of non-realistic geometry. Zhang *et al.* (2008) reported airflow and nanoparticle deposition in triple bifurcation units (G0-G3, G3-G6, etc.) up to 16 generations. They concluded that fully developed uniform nanoparticle concentration can be considered beyond generation 12 (G12). The study also showed that the geometric effects, including the *daughter branch rotation,* are insignificant for nanoparticles of less than 10nm in diameter.

Salma *et al*. (2015) studied pulmonary burden and ultrafine particle deposition distribution in stochastic pulmonary airways under different physical conditions. They concluded that the extrathoracic area of the lung receives the largest surface density deposition rate compared to other parts of the lung. Recently, Sohrabi et al. (2017) reported the ultrafine particle transport and delivery in a heterogeneous pulmonary network up to 16 generations. The authors considered a reconstructed model up to the 4th generation, and the artificially rebuilt pathway for the remaining 12 generations. In their model only a single truncated bifurcation throughout the 16 generations was considered which is far from the realistic branching pattern of the human respiratory system. Moreover, the single truncated bifurcation is not enough to predict the ultrafine particle TD in the terminal airways. Despite the high computational cost, it is important to consider the entire possible branching pattern of the human lung for a better understanding of the ultrafine particle TD in the complex bifurcating airways of the human lung. Until now there is no numerical or

analytical studies, which consider the whole branching pattern is available in the literature on ultrafine particle TD's for an entire lung model.

This study presents a more realistic, asymmetric, digital 17-generation lung model by considering the entire possible branching pattern. The computational mesh in the conduit- reconstructed anatomical model was generated from the Ansys 17.2 meshing module and studied a comprehensive ultrafine particle TD in the different lobes of a 17-generation branching conduit model. The current study also performs generation-by-generation pressure-drop throughout the 17-generations.

Numerical Methods

The current 17-generation anatomical airway model is the best available publication of the lung asymmetric model, as proposed by Schmidt *et al*. (2004). The present nanoparticle TD study is an extension of the CFD airflow study of Gemci *et al.* (2008) and microparticle TD study of Islam *et al*. (2017). An advanced meshing technique is used to generate the computational mesh. The details about the anatomical model and meshing can be found in Appendix A.

The viscous laminar model is used for the present study and the calculated maximum Reynolds number is 1620. The present study considers the anatomical model as derived from the trachea, which does not include the extrathoracic region. The flow behaviour at the extrathoracic region may be locally turbulent for $Q_{in} \geq 30\ lpm$ flow rates (Zhang and Kleinstreuer, 2004). However, the turbulence dispersion effects on nanoparticle deposition are found insignificant in the extrathoraic region (Zhang and Kleinstreuer, 2004, Longest and Xi, 2007, *Matida et al., 2004*) as well as the upper airways compared to microparticle deposition case (Zhang and Kleinstreuer, 2011b). A Lagrangian particle-tracking scheme is used to investigate the particle TD in the 17-generation

airways. Both Euler-Euler (E-E) and Euler-Lagrange (E-L) approaches are usually used for nanoparticle simulation. An E-E approach is used to solve convection-diffusion equations while an E-L approach solves particle trajectory equation. Shi *et al.*, 2008; Shi *et al.*, 2004; Zhang and Kleinstreuer, 2004; Zhang and Kleinstreuer, 2011a, all used the E-E method for nanoparticle modelling; whereas Aminfar and Motallebzadeh, 2012; Jayaraju *et al.*, 2008; Kalteh *et al.*, 2011; Longest and Xi, 2007 used E-L methods for nanoparticle simulation. The E-E approach treats both the continuous and the disperse phase as interpenetrating fields and usually neglects the particle inertia by considering the particle flow field effects and models particles as a dilute chemical species (Longest and Xi, 2007). The E-E method is suitable for tracking a large number of particles, however, inertial effects need to be introduced (De La Mora and Rosner, 1981). The E-L method tracks the individual particle trajectory by considering inertia, electrostatic effects, diffusivity, and near wall terms directly (Longest *et al.*, 2004). Despite better computational efficiency and higher resolution of the particle field of the E-E method, the present study uses the E-L approach as it also considers $d_p \geq 100nm$. An ANSYS 17.2 (FLUENT) solver-based Discrete Phase Model (DPM) is used to monitor the DEPM impact on the lung surface. The details about the air and particle transport equation discussions are reported in Appendix B.

Velocity inlet and pressure outlet boundary conditions were used. Zero pressure was set at all the outlets of the 17-generation model (Gemci et al., 2008; Koullapis et al., 2016; Luo and Liu, 2008; Sohrabi et al., 2017). At the wall surface of the anatomical model, a no-slip boundary condition was used (Luo and Liu, 2009). The Euler-Lagrange approach was used to solve the continuum gas phase and the disperse particle phase in DPM. SIMPLE, pressure-velocity coupling scheme and standard pressure spatial discretization were used. Second-order upwind momentum and energy spatial discretizations were used; and a hybrid initialization technique was used to initialise the

solution. The diesel exhaust particle with a density of 1100 kg/m^3 was considered; the particles were injected uniformly from the tracheal inlet surface area. All of the particles were injected at once. The tracking parameter length scale of 0.00005 was used in the present model (Inthavong et al., 2016).

The Lagrangian approach allows calculation of single particle trajectories using a force balance. Since the particulates occupy less than 1 percent of the volumetric fraction compared to the continuous phase, it is reasonable to consider the particulate phase as dilute in the human pulmonary airways. Based on Crowe et al. (2011) equations, the value for the momentum response time and collision time ratio in the study was 0.00041, which reasonably indicated that this is a one-way coupling problem.

A SGI Altix XE Cluster with 212 computational nodes and 960xE5-2680v3@2.5GHz 64bit Intel Xeon processor cores (12 core processors) was used for this numerical study. Each simulation of the present study took a minimum of 1,550 hours (CPU time) in the high performance computing unit. A total of 12 to 24 CPU's were used for each simulation.

Model Validation

The present 17-generation digital pulmonary lung model has been validated comprehensively with various published experimental data and CFD results. The present nanoparticle simulation results have been compared with the analytical solution in a straight pipe of different length, and the experimental data of a double bifurcation model. The present large-scale digital airway model has also been validated with various published CFD results.

Fig. 1 shows the nano-particle DE compared to the analytical results in a straight pipe of a different length (Gormley and Kennedy, 1948; Ingham, 1975). The numerical result for a wide range of

nanoparticle ($5 \leq dp \leq 100$) deposition shows good agreement with the published analytical solutions.

Fig. 2 shows the nano-particle DE compared with experimental results of a double bifurcation model (G3-G5) of Kim (2002). The present results were validated for the first and second bifurcation of G3-G5 generations. The current model has also been compared with the CFD results of Zhang and Kleinstreuer (2004) for a different inlet Reynolds number (Re = 200, 500 and 1000). Fig. 2(a) shows comparison of nano-particle deposition for the first bifurcation; and Fig. 2(b) shows the deposition comparison for the second bifurcation. The present nano-particle DE shows good agreement with the published experimental data for both bifurcations.

Table. 1: Percentage variation comparison between flow rate in different lobes with available published data (Cohen *et al*., 1990; Horsfield *et al.*, 1971)

Total Flow Distribution (%)			
Region	Cohen *et al.* (1990) 7.5 lpm	Present 7.5 lpm	Horsfield *et al.* (1971)
Left lower	24.5	25.14	24.9
Left upper	14.9	15.34	20.5
Right lower	32.1	36.17	23.2
Right middle	8.3	11.01	9.6
Right upper	20.2	12.48	21.7
Left lung	39.4	40.48	45.4
Right lung	60.6	59.66	54.6

Table 1 shows the total flow rate distribution percentage comparison across five different lobes of the entire anatomical lung model with the benchmark published data (Cohen *et al*., 1990; Horsfield *et al*., 1971). Table 1 shows the total flow distribution at 7.5 lpm flow rate. The available published measurement for 7.5 lpm flow rate (Cohen *et al.*, 1990) shows excellent agreement for total flow distribution at the right and left lung of the present study. At 7.5 lpm flow rate, the percentage of the flow distribution at the left lung is 40.48 percent, the right lung is 59.66 percent. Total flow distribution comparison with the benchmark published measurement shows good agreement, indicating that the present CFD model is sufficiently accurate.

DE trend comparison at the different lobes of the 17-generation digital airway model with the analytical MPPD model is shown in Fig. 3. The analytical model shows higher deposition at the left lower lobe and the lower deposition at the right middle lobe, which is also similar to the DE of the present CFD model. The DE trend of the remaining lobes of the 17-generation airway model also shows good agreement with the DE trend of the MPPD model. The five-lobe analytical model is used for the DE of the MPPD model (Yeh and Schum, 1980). The overall DE trend of the analytical MPPD model supports the DE trend of the present CFD model and eventually proves that the present model is sufficiently accurate to predict lobar deposition for the ultrafine particle.

In summary, good agreement between the current results and the published results indicates that the current model is sufficiently accurate to predict the nanoparticle TD in the 17-generation model.

Results and Discussions

The current study accounts for ultrafine particle TD in a 17-generation lung model and performs a comprehensive ultrafine particle TD in a lung model under conditions of sleeping, resting, and

light activity. 7.5 lpm, 9 lpm, and 25 lpm flow rates are considered for these three conditions, respectively, based on the ICRP 1994 standard (ICRP and Protection, 1994). The present large-scale model considered a wide range of ultrafine particles ($1 \leq nm \leq 1000$) to predict smaller diameter particle deposition in the deeper airways.

Pressure-gradient in the bifurcating branches of the human lung is important for the total respiratory process; the bifurcating airways cause resistance in order to transport air throughout the respiratory process (Chovancová and Elcner, 2014). Understanding the pressure-drop throughout the five different lobes of the pulmonary airways is essential for pharmaceutical aerosol particle TD in the pulmonary airways. Because of the complex anatomical structure of the pulmonary airways, airway resistance in the five different lobes should be different. Five randomly selected path lines along five different lobes of the 17-generation anatomical model can be found in Appendix C.

Fig. 4 shows the pressure-drop variation along the five selected path lines for five different lobes of the 17-generation model. The pressure-drop has been conducted for three different flow rates. Fig. 4 shows the pressure-drop variation for 7.5 lpm, 9 lpm, and 25 lpm flow rates, respectively. The overall pressure-drop for different lobes shows a non-linear behaviour throughout the 17-generation. The pressure-drop at the right lower lobe shows fluctuation at the 4^{th}-5^{th} generation.

Fig. 5 shows the 1-nm diameter nanoparticle deposition pattern in the 17-generation airway model for the different flow rates. The overall deposition pattern shows that the Brownian motion is effective for smaller diameter particles and lower flow rates. Note that Brownian motion is the random microscopic motion of the gas molecules, and gas molecules collision cause the diffusion. The effect of the Brownian motion increases with the decrease in particle diameter and flow rates.

Under sleep conditions (Fig. 5a, 7.5lpm flow rate), higher numbers of 1-nm diameter particles are deposited at the tracheobronchial airways than under resting conditions (Fig. 5b, 9 lpm flow rate). During conditions of light activity (25 lpm flow rate), ultrafine particle deposition is noticeably lower in the tracheobronchial airways than under sleeping and resting conditions. The deposition scenario of the 1-nm diameter particle is found to be inversely proportional to the flow rates. The overall deposition pattern for the 1-nm diameter particle also satisfies the general assumption of Brownian motion of the ultrafine particle. The overall deposition pattern shows that Brownian motion is dominant in the upper airways, depending on the lower flow rates. The DE of the ultrafine particle decreases with increased diameter as the diffusive capacity of the particle decreases with the increase of the diameter. On the contrary, the DE of the ultrafine particle at higher flow rate decreases because of its lower residence time. The deposition scenario of the 1-nm diameter particle satisfies the general assumption of diffusion and shows higher deposition at the upper airways. The DE of the ultrafine particles increases with increased diffusion parameter. The diffusion parameter, Δ is a function of inhalation flow rate, geometrical dimension, and the particle properties, which can be defined as;

$$\Delta = \frac{\pi \tilde{D} L}{4Q} \tag{1}$$

where $\tilde{D}$ is nano-particle diffusivity, L is the length of the domain, and Q is the flow rate. For 1-nm particle, the diffusivity value is 0.0534 cm^2/s; the diffusion parameter value for 1-nm diameter particle is calculated for different flow rates. Table 2 shows the diffusion parameter value for conditions of sleep, rest, and light activity in the present study.

Table. 2: Diffusion parameter value for different physical conditions

	7.5 lpm	9 lpm	25 lpm
Diffusion Parameter (Δ)	0.00369	0.003075	0.001107

Table 2 shows that diffusion parameter value decreases with increased flow rate for the 1-nm particle, which also supports the higher deposition during sleeping conditions. A comprehensive deposition pattern for 10-nm and 50-nm diameter particle is also investigated.

Fig. 6 shows deposition concentration comparison at the left and right lung for different diameter particles. The overall deposition density curve shows the particle deposition concentration in different parts of the left and right lung for different physical condition. The deposition density curve shows the deposition hot spot for different diameter ultrafine particles in the right and left lung. Fig. 6(a) shows the deposition hot spot for the 1-nm diameter particle in the upper portion of the tracheobronchial airways. Higher numbers of 1-nm diameter particles are deposited at the tracheal parent tube and the right upper lobe. Figs. 6(b, c, d) show that the deposition concentrations of 10-nm, 50-nm, and 1000-nm respectively diameter particles in the right lung are higher at the middle and lower lobes. For the left lung however, the deposition concentration is higher at the left lower lobe.

Fig. 7 shows a comprehensive lobar deposition density comparison for a wide range of ultrafine particles under different physical conditions. Fig. 7(a) shows the deposition density comparison for different diameter particles in the right upper lobe. The deposition-density curve clearly shows that the middle portion of the right upper lobe is the deposition hot spot for ultrafine particles. The deposition density curve shows a significant amount of 1-nm diameter particles deposited in the

middle of the right upper lobe. Fig. 7(a) also depicts that the deposition concentration in the right upper lobe decreases with increases of the nanoparticle diameter and flow rate. Fig. 7(b) compares deposition density in the right middle lobe of the 17-generation bifurcating model. The density curve shows different hot spots for various diameter particles in the right middle lobe under various flow rates. Fig. 7(c) compares the deposition density in the right lower lobe of the 17-generation anatomical model. The overall deposition density curve displays different hot spots for various flow rates. The density curve shows higher deposition at the upper portion of the right lower lobe for 1-nm particles; however, the deposition hot spot is in the middle of the right lower lobe for 10-nm and 50-nm diameter particles. Fig. 7(d) shows the deposition density comparison in the left upper lobes; and the overall deposition shows a similar deposition pattern like the right upper lobe. Fig. 7(e) shows the deposition density comparison in the left lower lobe; and the density curve clearly shows the unlike deposition behaviour, irrespective of particle diameter and flow rate. The comprehensive lobar deposition density comparison for a 17-generation lung model shows different deposition hot spots for different lobes. The lobar deposition density comparison, as a function of different deposition parameter, could fill the lack of nano-particle deposition data for a whole lung model. The unlike deposition concentration data in the different lobes could help to determine the relevance of the clinical and biological findings. The size-specific ultrafine particle deposition information during different physical conditions will increase the understanding of the potential health risk estimations.

The nano-particle DE comparison in the different lobes of the 17-generation anatomical model at different flow rates is shown in Fig. 8. The DE in the different lobes of the right and left lung is unlike irrespective of particle diameter and flow rates. Overall DE comparison shows higher deposition concentration in the right lower lobes and lower deposition concentration in the left

upper lobes. Figs. 8(a, b, c) clearly show distinct lobar deposition for different diameter particles at different flow rates. Parkash (1977) investigated that the lung cancer carcinomas, mostly formed at the right lung rather than the left lung, and more precisely at the lower lobes instead of the upper lobes of the pulmonary airways. The diesel exhaust particles and cigarette smoke are carcinogens, but not all ultrafine particles are designated as carcinogens. The inhaled toxic and ultrafine particles can reach the terminal bronchioles of the deeper airways and depending on their residence time these ultrafine particle can develop cancer arising carcinomas. In this regard, more comprehensive lobar deposition investigation is necessary to predict and preclude the presence of lung cancer. The present 17-generation digital airway model allows comprehensive nanoparticle deposition data at the different lobes, which could potentially increase understanding of lobar deposition and, more specifically, transport of nanoparticles to the targeted drug delivery system.

Conclusions

The present 17-generation digital anatomical model illustrates comprehensive ultrafine particle TD throughout the possible entire branching pattern of the human lung. The present numerical model considers ultrafine particles ranging from $1 \leq nm \leq 1000$ diameter for sleep, resting and light activities physical condition. A comprehensive validation has been performed and the following conclusions are drawn from the present study:

- The percentage distribution of total flow rate in the right lung is about 1.5 times higher than at the left lung for this study. More specifically, the flow rate at the lower lobes of the right and the left lung is higher than in other lobes.

- The pressure drop along the selected path of the five different lobes shows a non-linear trend for different flow rates. The pressure drop at the right lower lobe shows more fluctuations compared to the other lobe.
- Particles diameter of $d_p \leq 10nm$ are deposited at the tracheobronchial airways. On contrary, particles greater than 10-nm in diameter are deposited at the terminal bronchioles of the anatomical model.
- The ultrafine particle deposition density curve shows the deposition hot spot at the left and the right lungs for different deposition parameter. More specifically, different lobar deposition hot spots were observed for different diameter particles.
- At 7.5 lpm flow rate, 1-nm diameter particle DE is higher at the right lower lobe, whereas 1-nm diameter particle DE is lower at the left upper lobe. For the same flow rate, DE of particles greater than 10-nm is higher at the left lower lobe. At 9 lpm flow rate, particles with a diameter greater than 50-nm are mostly deposited at the right upper and left lower lobes. At 25 lpm flow rate, 50-nm diameter particle DE is higher at the right lower lobe, whereas 50-nm diameter particle DE is lower at the left upper lobe.

The advanced first ever ultrafine particles modelling up to 17-generation of a bifurcating model will increase the knowledge of the pharmaceutical aerosol TD in the terminal bronchioles. The inclusive pressure-drop analysis throughout the 17-generations along five selected line in five different lobes, will advance the understanding of the health risk assessment of patients with respiratory diseases. The comprehensive particle deposition density analysis in different lobes would increase the lobar deposition knowledge and might be an important step to overcome the lack of the ultrafine particle deposition data in the terminal bronchioles. The present findings would potentially help the targeted drug delivery system design and increase the efficiency of the

drug delivery to the specific positions in the pulmonary airways. The current study together with more specific case studies, would increase the clinically and biologically relevant knowledge of the zone-specific drug delivery into the terminal bronchioles and the alveolar sac region of the whole lung model. These models could potentially lead to the improvement of novel therapies for the different respiratory diseases. More specially, the comprehensive lobar deposition model could be useful in the design of a zone-specific drug delivery device for lung cancer patients. A comprehensive ultrafine polydispersed particle TD for a whole lung model will be examined next.

Acknowledgement

The authors would like to thank the financial support received from the ARC Discovery Project (DP150100828) and ARC Linkage Project (LP150100737). The authors gratefully acknowledge the use of the high-performance computing (HPC) unit, of Queensland University of Technology (QUT). The interpretations and conclusions contained in this study are those of the authors and should not be interpreted as necessarily representing the official policies or endorsements either expressed or implied, of QUT or of the firm B. Braun Medical Inc.

Conflict of interest statement

The authors declare no conflict of interest.

Appendix

A. Geometry and Meshing

The present 17-generation digital airway model exhibits strong asymmetry and multi-fractal properties. The branching pattern and carinal angle throughout the 17-generation anatomical model are highly asymmetric. The anatomical graph data of the digital reference model is derived

from the high-resolution CT imaging of an *in vitro* arrangement, with specifically adapted image processing algorithm to portray and segment the bronchi. The digital airway model contains 1452 bronchi, up to the 17-generation Horsfield order, including the central and lower tracheobronchial airways. The tracheal inlet area of the current model was 162.68 $mm^{2,}$ and the tracheal inlet diameter 14.4 mm.

B. Air Flow Pattern

Fig. A1 represents the velocity magnitude contours at a randomly selected cross-section area of the 17-generation bronchial tree model. Fig. A1(a) and Fig. A1(b) present velocity magnitude contours for 7.5 lpm and 25 lpm flow rates, respectively. Overall, velocity magnitude contour shows that the flow rate in the right bronchus is greater than that in the left bronchus. The different diameters of the right and left bronchus tubes, different lengths, and the highly asymmetric structures, influence the flow rate; the right lung reaches maximal velocity in both cases. At 7.5 lpm flow, maximum velocity is 1.030 m/s, and maximum velocity is 3.139 m/s at 25 lpm flow rate. In the right lung, the maximum velocity develops at lower bronchus G2 and the right lower lobes. The randomly selected cross-sectional planes are parallel to the tracheal inlet of the 17-generation model.

B. Mathematical Formulations

The following mass and momentum equations respectively were solved to calculate air flow.

$$\frac{\partial \rho}{\partial t} + \nabla \cdot \left(\rho \vec{v} \right) = S_m \tag{A1}$$

where S_m is the mass source term.

$$\frac{\partial}{\partial t}(\rho \vec{v}) + \nabla \cdot (\rho \vec{v}\vec{v}) = -\nabla p + \nabla \cdot \left(\mu \left[\left(\nabla \vec{v} + \nabla \vec{v}^T \right) - \frac{2}{3} \nabla \cdot \vec{v} I \right] \right) + \rho \vec{g} + \vec{F} \quad \text{(A2)}$$

where, p is fluid static pressure, $\rho \vec{g}$ is body force due to gravity, μ is the molecular viscosity, I is the unit tensor, and $\vec{F}$ is body force due to external force (particle-fluid interaction). A pressure-velocity coupling scheme, SIMPLE was used to solve the DPM particle movement. A parabolic inlet condition for laminar flow (White, 2003) was used

$$u(r) = 2u_{av}\left(1 - \frac{r^2}{R^2}\right) \quad \text{(A3)}$$

where R is the airway inlet radius.

To model the nano-particles, Brownian motion was considered. An appropriate particle motion equation (Inthavong *et al.*, 2009) was solved to calculate the individual particles.

$$\frac{du_i^p}{dt} = F_D(u_i^g - u_i^p) + F_{Brownian} + F_{Lift} + \frac{\rho_p - \rho_g}{\rho_p} g_i$$

$$F_D = \frac{18\mu_g}{\rho_p d_p^2 C_c} \quad \text{(A4)}$$

$$C_c = 1 + \frac{2\lambda}{d_p}(1.257 + 0.4e^{-1.1 d_p / 2\lambda})$$

where F_D is the drag force per unit particle mass, and C_c is the Cunningham correction factor. The specific correction factor values were used for different diameter particle. λ is the mean free path of the gas molecules. The Brownian force amplitude is defined as

$$F_{Brownian} = \zeta \sqrt{\frac{\pi S_0}{\Delta t}} \quad \text{(A5)}$$

where ζ is the unit variance independent Gaussian random number, Δt is the particle time-step integration. The spectral intensity (S_0) by a Gaussian white noise random process is defined as

$$S_o = \frac{216\mu k_B T}{\pi^2 \rho_p d_p^{\,5} (\frac{\rho_p}{\rho_g})^2 C_c} \tag{A6}$$

T is the fluid absolute temperature, k_B is the Boltzmann constant, ρ_g is the gas density.

The Saffman's lift force is used (Li and Ahmadi, 1992), which is a generalization of the Saffman expression (Saffman, 1965).

$$F_{Lift} = \frac{2Kv^{1/2}\rho d_{ij}}{\rho_p d_p (d_{lk} d_{kl})^{1/4}} (\rho - \rho_p) \tag{A7}$$

where K=2.594 and d_{ij} is the deformation tensor.

C. Results and Discussion

Fig. A2 shows the five randomly selected path lines along five different lobes of the 17-generation anatomical model.

Limitations of the study

The human breathing pattern is very complicated depending on the conditions related to different physical activities. Breathing includes a cycle of inhalations and exhalations. Under normal conditions, breathing rate is automatically controlled by homeostasis but over breathing or under breathing can provoke different medical problems. Particle transport and deposition predictions for a large scale model are complex from different aspects. The authors endeavoured to make the total approach less complicated by considering only inhalation effects in the present study and did

not consider exhalation effect. In almost all of the published in silico and in vivo studies parabolic or uniform inlet velocity condition were assumed in the models. In reality, the inlet velocity profile is quite complicated because of flow properties and geometrical asymmetricity. To avoid complicated inlet condition, a fully developed parabolic inlet velocity was used in the present large scale model. The authors also assumed zero pressure at the 17-geneartion outlet. In reality, there is a small pressure difference at the outlet of the terminal airways for a whole lung model. The present model considered first 17 generations of the pulmonary airways. Therefore, open outlet condition (zero pressure) is used at the outlet.

References

Aminfar, H., Motallebzadeh, R., 2012. Investigation of the velocity field and nanoparticle concentration distribution of nanofluid using Lagrangian-Eulerian approach. Journal of Dispersion Science and Technology 33, 155-163.

Asgharian, B., Price, O.T., 2007. Deposition of ultrafine (nano) particles in the human lung. Inhalation toxicology 19, 1045-1054.

Cheng, K.-H., Cheng, Y.-S., Yeh, H.-C., Guilmette, R.A., Simpson, S.Q., Yang, Y.-H., Swift, D.L., 1996. In vivo measurements of nasal airway dimensions and ultrafine aerosol deposition in the human nasal and oral airways. Journal of Aerosol Science 27, 785-801.

Cheng, Y.-S., Yamada, Y., Yeh, H.-C., Swift, D.L., 1988. Diffusional deposition of ultrafine aerosols in a human nasal cast. Journal of Aerosol Science 19, 741-751.

Chovancová, M., Elcner, J., Year The pressure gradient in the human respiratory tract. In EPJ Web of Conferences.

Cohen, B.S., Sussman, R.G., Lippmann, M., 1990. Ultrafine particle deposition in a human tracheobronchial cast. Aerosol Science and Technology 12, 1082-1091.

Crowe, C.T., Schwarzkopf, J.D., Sommerfeld, M., Tsuji, Y., 2011. Multiphase flows with droplets and particles. CRC press.

De La Mora, J.F., Rosner, D., 1981. Inertial deposition of particles revisited and extended: Eulerian approach to a traditionally Lagrangian problem. PhysicoChemical Hydrodynamics 2, 1-21.

Diat-Sanchez, D., 1997. The role of diesel exhaust particles and their associated polyaromatic hydrocarbons in the induction of allergic airway disease. Allergy 52, 52-56.

Farhadi Ghalati, P., Keshavarzian, E., Abouali, O., Faramarzi, A., Tu, J., Shakibafard, A., 2012. Numerical analysis of micro- and nano-particle deposition in a realistic human upper airway. Comput Biol Med 42, 39-49.

Frampton, M.W., 2001. Systemic and cardiovascular effects of airway injury and inflammation: ultrafine particle exposure in humans. Environmental health perspectives 109, 529.

Gehr, P., Heyder, J., 2000. Particle-lung interactions. CRC Press.

Gemci, T., Ponyavin, V., Chen, Y., Chen, H., Collins, R., 2008. Computational model of airflow in upper 17 generations of human respiratory tract. Journal of Biomechanics 41, 2047-2054.
Gormley, P., Kennedy, M., 1948. Diffusion from a stream flowing through a cylindrical tube. Proceedings of the Royal Irish Academy. Section A: Mathematical and Physical Sciences, 163-169.
Horsfield, K., Dart, G., Olson, D.E., Filley, G.F., Cumming, G., 1971. Models of the human bronchial tree. Journal of Applied Physiology 31, 207-217.
Hsiao, I.-L., Huang, Y.-J., 2013. Effects of serum on cytotoxicity of nano-and micro-sized ZnO particles. Journal of Nanoparticle Research 15, 1829.
ICRP, Protection, I.C.o.R., 1994. ICRP Publication 66: Human Respiratory Tract Model for Radiological Protection. Elsevier Health Sciences.
Ingham, D., 1975. Diffusion of aerosols from a stream flowing through a cylindrical tube. Journal of Aerosol Science 6, 125-132.
Inthavong, K., Tian, L., Tu, J., 2016. Lagrangian particle modelling of spherical nanoparticle dispersion and deposition in confined flows. Journal of Aerosol Science 96, 56-68.
Inthavong, K., Tu, J., Ahmadi, G., 2009. Computational modelling of gas-particle flows with different particle morphology in the human nasal cavity. The Journal of Computational Multiphase Flows 1, 57-82.
Inthavong, K., Zhang, K., Tu, J., 2011. Numerical modelling of nanoparticle deposition in the nasal cavity and the tracheobronchial airway. Computer Methods in Biomechanics and Biomedical Engineering 14, 633-643.
Islam, M.S., Saha, S.C., Sauret, E., Gemci, T., Gu, Y., 2017. Pulmonary aerosol transport and deposition analysis in upper 17 generations of the human respiratory tract. Journal of Aerosol Science 108, 29-43.
Jayaraju, S., Brouns, M., Lacor, C., Belkassem, B., Verbanck, S., 2008. Large eddy and detached eddy simulations of fluid flow and particle deposition in a human mouth–throat. Journal of Aerosol Science 39, 862-875.
Kalteh, M., Abbassi, A., Saffar-Avval, M., Harting, J., 2011. Eulerian–Eulerian two-phase numerical simulation of nanofluid laminar forced convection in a microchannel. International Journal of Heat and Fluid Flow 32, 107-116.
Kim, C., 2002. Ultrafine particle deposition in a double bifurcation tube with human G3–G5 airway geometry. US EPA, Internal Report.
Koullapis, P., Kassinos, S., Bivolarova, M.P., Melikov, A.K., 2016. Particle deposition in a realistic geometry of the human conducting airways: Effects of inlet velocity profile, inhalation flowrate and electrostatic charge. Journal of biomechanics 49, 2201-2212.
Laumbach, R.J., Kipen, H.M., 2012. Respiratory health effects of air pollution: update on biomass smoke and traffic pollution. Journal of allergy and clinical immunology 129, 3-11.
Lee, J.H., Lee, J.Y., Yu, I.J., 2011. Developing Korean standard for nanomaterial exposure assessment. Toxicological research 27, 53.
Li, A., Ahmadi, G., 1992. Dispersion and deposition of spherical particles from point sources in a turbulent channel flow. Aerosol science and technology 16, 209-226.
Longest, P.W., Kleinstreuer, C., Buchanan, J.R., 2004. Efficient computation of micro-particle dynamics including wall effects. Computers & Fluids 33, 577-601.
Longest, P.W., Xi, J., 2007. Effectiveness of direct Lagrangian tracking models for simulating nanoparticle deposition in the upper airways. Aerosol Science and Technology 41, 380-397.

Luo, H., Liu, Y., 2008. Modeling the bifurcating flow in a CT-scanned human lung airway. Journal of Biomechanics 41, 2681-2688.
Luo, H., Liu, Y., 2009. Particle deposition in a CT-scanned human lung airway. Journal of biomechanics 42, 1869-1876.
Matida, E., Finlay, W., Lange, C., Grgic, B., 2004. Improved numerical simulation of aerosol deposition in an idealized mouth–throat. Journal of Aerosol Science 35, 1-19.
Moskal, A., Gradoń, L., 2002. Temporary and spatial deposition of aerosol particles in the upper human airways during breathing cycle. Journal of Aerosol Science 33, 1525-1539.
Oberdörster, G., 2000. Pulmonary effects of inhaled ultrafine particles. International archives of occupational and environmental health 74, 1-8.
Parkash, O., 1977. Lung cancer. Respiration 34, 295-304.
Rothen-Rutishauser, B.M., Kiama, S.G., Gehr, P., 2005. A three-dimensional cellular model of the human respiratory tract to study the interaction with particles. American journal of respiratory cell and molecular biology 32, 281-289.
Saffman, P., 1965. The lift on a small sphere in a slow shear flow. Journal of fluid mechanics 22, 385-400.
Salma, I., Füri, P., Németh, Z., Balásházy, I., Hofmann, W., Farkas, Á., 2015. Lung burden and deposition distribution of inhaled atmospheric urban ultrafine particles as the first step in their health risk assessment. Atmospheric Environment 104, 39-49.
Schmidt, A., Zidowitz, S., Kriete, A., Denhard, T., Krass, S., Peitgen, H.-O., 2004. A digital reference model of the human bronchial tree. Computerized Medical Imaging and Graphics 28, 203-211.
Shi, H., Kleinstreuer, C., Zhang, Z., 2006. Laminar airflow and nanoparticle or vapor deposition in a human nasal cavity model. Journal of biomechanical engineering 128, 697-706.
Shi, H., Kleinstreuer, C., Zhang, Z., 2008. Dilute suspension flow with nanoparticle deposition in a representative nasal airway model. Physics of Fluids 20, 013301.
Shi, H., Kleinstreuer, C., Zhang, Z., Kim, C., 2004. Nanoparticle transport and deposition in bifurcating tubes with different inlet conditions. Physics of Fluids (1994-present) 16, 2199-2213.
Sohrabi, S., Wang, S., Tan, J., Xu, J., Yang, J., Liu, Y., 2017. Nanoparticle transport and delivery in a heterogeneous pulmonary vasculature. Journal of Biomechanics 50, 240-247.
Swift, D.L., Montassier, N., Hopke, P.K., Karpen-Hayes, K., Cheng, Y.-S., Su, Y.F., Yeh, H.C., Strong, J.C., 1992. Inspiratory deposition of ultrafine particles in human nasal replicate cast. Journal of aerosol science 23, 65-72.
White, F.M., 2003. Fluid mechanics. 5th. Boston: McGraw-Hill Book Company.
Xi, J., Longest, P.W., 2008a. Effects of oral airway geometry characteristics on the diffusional deposition of inhaled nanoparticles. Journal of biomechanical engineering 130, 011008.
Xi, J., Longest, P.W., 2008b. Numerical predictions of submicrometer aerosol deposition in the nasal cavity using a novel drift flux approach. International Journal of Heat and Mass Transfer 51, 5562-5577.
Yeh, H.-C., Schum, G.M., 1980. Models of human lung airways and their application to inhaled particle deposition. Bulletin of Mathematical Biology 42, 461-480.
Yu, G., Zhang, Z., Lessmann, R., 1996. Computer simulation of the flow field and particle deposition by diffusion in a 3-D human airway bifurcation. Aerosol Science and Technology 25, 338-352.
Zhang, Z., Kleinstreuer, C., 2004. Airflow structures and nano-particle deposition in a human upper airway model. Journal of computational physics 198, 178-210.

Zhang, Z., Kleinstreuer, C., 2011a. Computational analysis of airflow and nanoparticle deposition in a combined nasal–oral–tracheobronchial airway model. Journal of Aerosol Science 42, 174-194.
Zhang, Z., Kleinstreuer, C., 2011b. Laminar-to-turbulent fluid–nanoparticle dynamics simulations: model comparisons and nanoparticle-deposition applications. International Journal for Numerical Methods in Biomedical Engineering 27, 1930-1950.
Zhang, Z., Kleinstreuer, C., Donohue, J.F., Kim, C., 2005. Comparison of micro-and nano-size particle depositions in a human upper airway model. Journal of aerosol science 36, 211-233.
Zhang, Z., Kleinstreuer, C., Kim, C.S., 2008. Airflow and nanoparticle deposition in a 16-generation tracheobronchial airway model. Annals of biomedical engineering 36, 2095-2110.

Figure Captions

Fig. 1: DE comparison with analytical results of Gormley and Kennedy (1948) , Ingham (1975) in a straight pipe of different length at 1 m/s inlet velocity

Fig. 2: Nano-particle DE comparison with the experimental data of Kim, 2002 and the CFD results of Zhang and Kleinstreuer, 2004, in a double bifurcation model (G3-G5), (a) first bifurcation, and (b) second bifurcation.

Fig. 3: DE trend comparison at the different lobes of the 17-generation model with the analytical Multiple-Path Particle Dosimetry (MPPD) model: (a) present CFD model results and (b) analytical MPPD model results.

Fig. 4: Pressure drop variation along five selected path lines for five different lobes with different flow rates, (a) 7.5 lpm, (b) 9 lpm, and (c) 25 lpm

Fig. 5: Respiratory deposition pattern of 1-nm particle up to the 17-generation of the digital asymmetric airway model: (a) 7.5 lpm flow rate, (b) 9 lpm flow rate, and (c) 25 lpm flow rate.

Fig. 6: Particle deposition concentration comparison in the left and right lung under sleeping, resting and light activity conditions for (a) 1-nm, (b) 10-nm, (c) 50-nm, and (d) 1000-nm diameter particles

Fig. 7: Deposition density comparison with different lobes as a function of particle diameter and flow rates, (a) right upper lobes, (b) right middle lobes, (c) right lower lobes, (d) left upper lobes, and (e) left lower lobes

Fig. 8: DE comparisons for nanoparticles of various diameters at different lobes of the right and the left lung, (a) 7.5 lpm flow rate, (b) 9 lpm flow rate, and (c) 25 lpm flow rate

Figure Captions: Appendix

Fig. A1: Velocity contour across the 17-generation bifurcation airways for different volumetric flow rates, (a) 7.5 lpm, and (b) 25lpm

Fig. A2: Pressure drop variation for five selected path lines along five different lobes

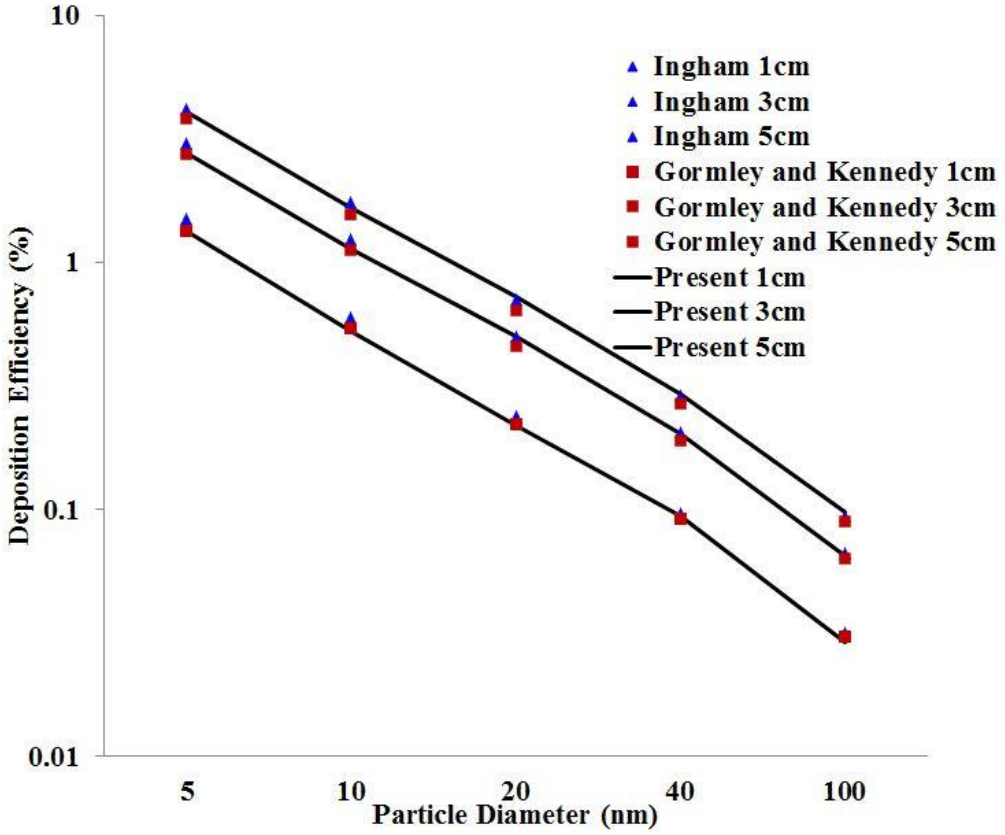
10
1
0.1
0.01
Deposition Efficiency (%)
5
10
20
40
100
Particle Diameter (nm)
Ingham 1cm
Ingham 3cm
Ingham 5cm
Gormley and Kennedy 1cm
Gormley and Kennedy 3cm
Gormley and Kennedy 5cm
Present 1cm
Present 3cm
Present 5cm

Fig. 1

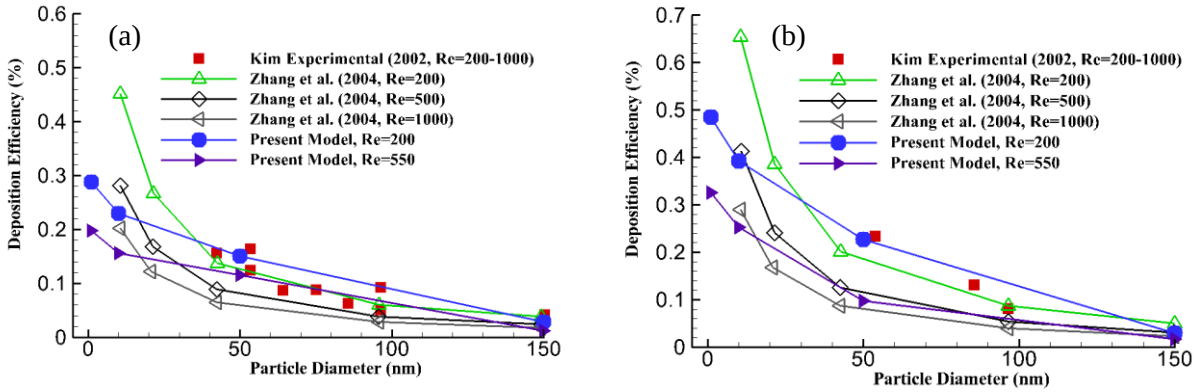
(a)
Kim Experimental (2002, Re=200-1000)
Zhang et al. (2004, Re=200)
Zhang et al. (2004, Re=500)
Zhang et al. (2004, Re=1000)
Present Model, Re=200
Present Model, Re=550
Deposition Efficiency (%)
Particle Diameter (nm)
0
0.1
0.2
0.3
0.4
0.5
0.6
50
100
150
(b)
Kim Experimental (2002, Re=200-1000)
Zhang et al. (2004, Re=200)
Zhang et al. (2004, Re=500)
Zhang et al. (2004, Re=1000)
Present Model, Re=200
Present Model, Re=550
Deposition Efficiency (%)
Particle Diameter (nm)
0
0.1
0.2
0.3
0.4
0.5
0.6
0.7
50
100
150

Fig. 2

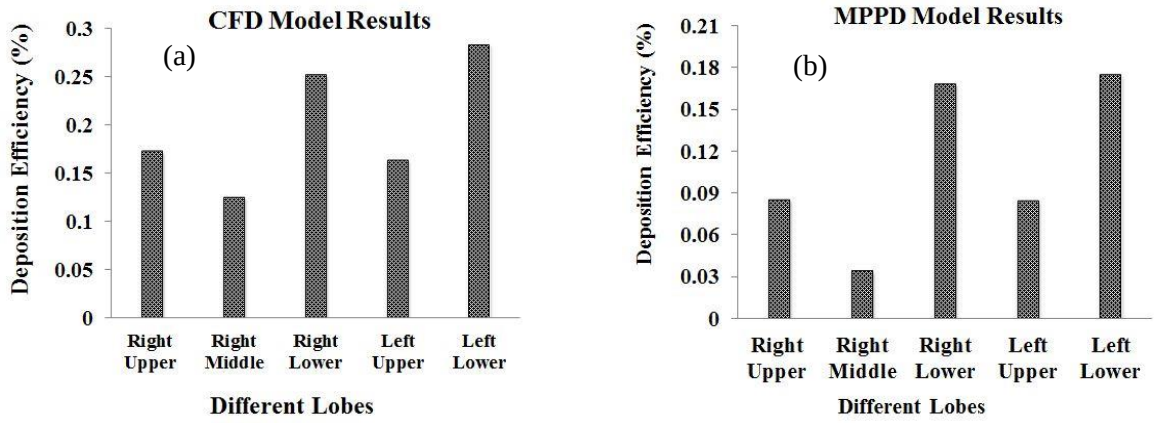
CFD Model Results
(a)
Deposition Efficiency (%)
0.3
0.25
0.2
0.15
0.1
0.05
0
Right Upper
Right Middle
Right Lower
Left Upper
Left Lower
Different Lobes
MPPD Model Results
(b)
Deposition Efficiency (%)
0.21
0.18
0.15
0.12
0.09
0.06
0.03
0
Right Upper
Right Middle
Right Lower
Left Upper
Left Lower
Different Lobes

Fig. 3

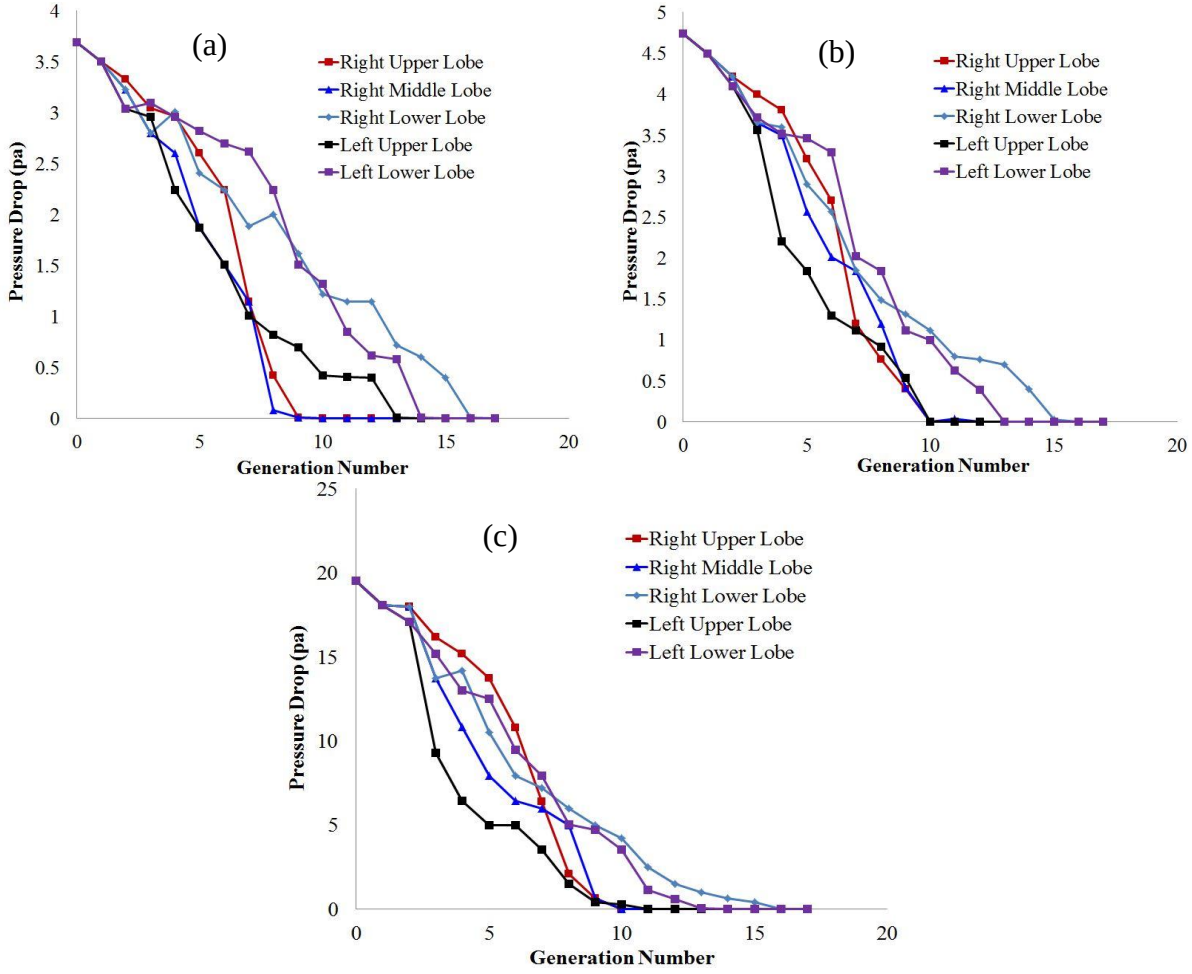
(a)
Right Upper Lobe
Right Middle Lobe
Right Lower Lobe
Left Upper Lobe
Left Lower Lobe
Pressure Drop (pa)
Generation Number
(b)
Right Upper Lobe
Right Middle Lobe
Right Lower Lobe
Left Upper Lobe
Left Lower Lobe
Pressure Drop (pa)
Generation Number
(c)
Right Upper Lobe
Right Middle Lobe
Right Lower Lobe
Left Upper Lobe
Left Lower Lobe
Pressure Drop (pa)
Generation Number

Fig. 4

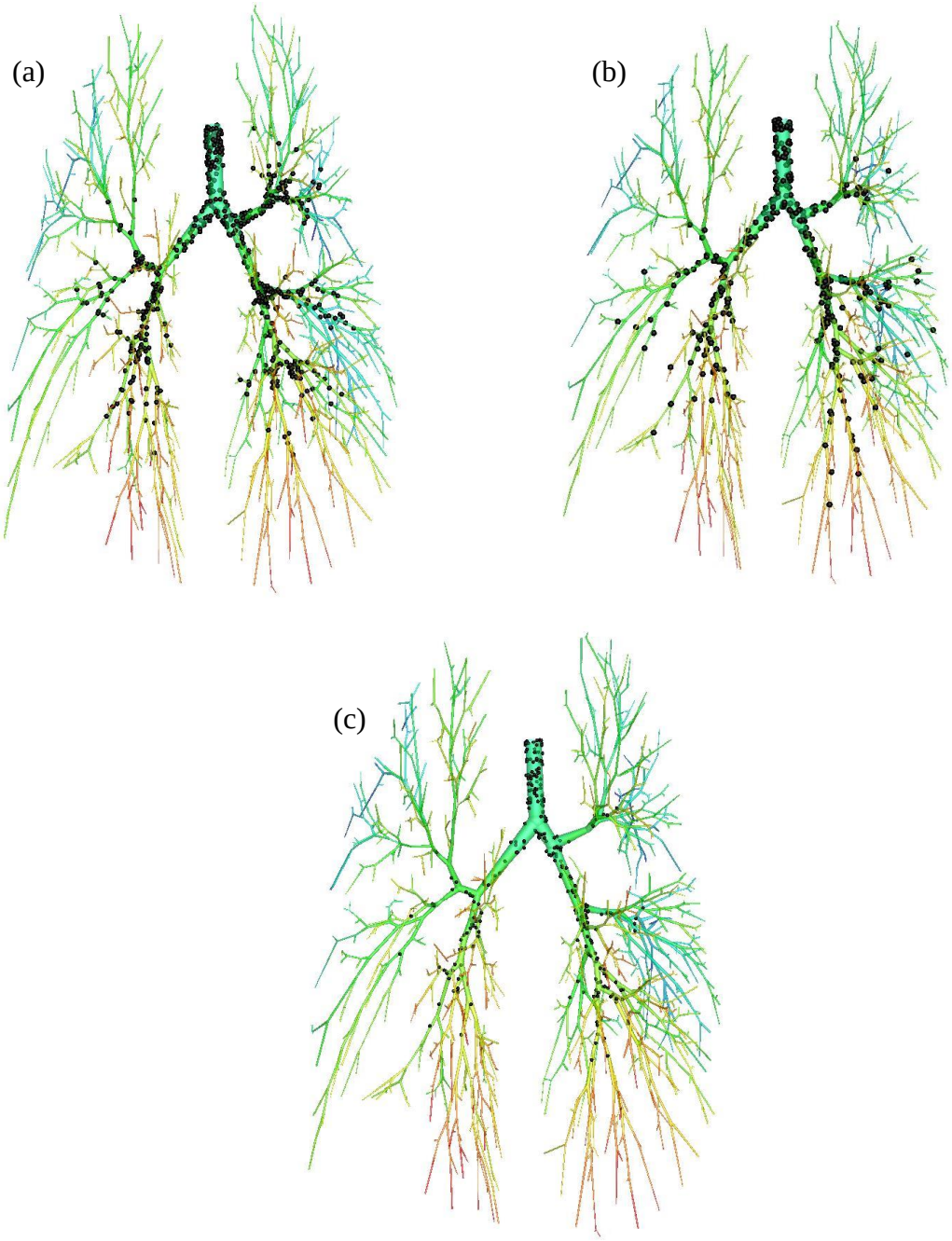

Fig. 5

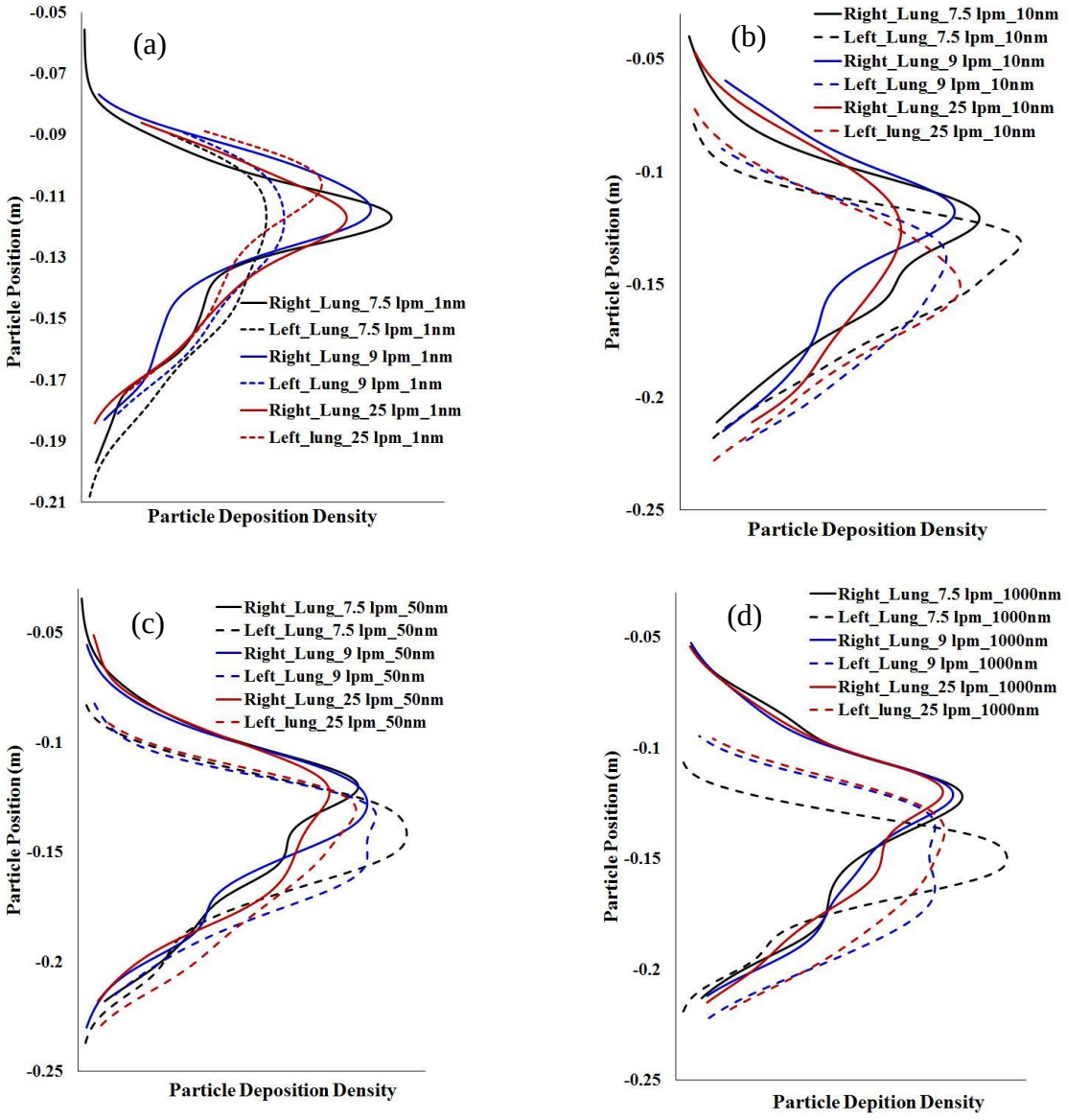
(a)
Particle Position (m)
-0.05
-0.07
-0.09
-0.11
-0.13
-0.15
-0.17
-0.19
-0.21
Particle Deposition Density
Right_Lung_7.5 lpm_1nm
Left_Lung_7.5 lpm_1nm
Right_Lung_9 lpm_1nm
Left_Lung_9 lpm_1nm
Right_Lung_25 lpm_1nm
Left_lung_25 lpm_1nm
(b)
Particle Position (m)
-0.05
-0.1
-0.15
-0.2
-0.25
Particle Deposition Density
Right_Lung_7.5 lpm_10nm
Left_Lung_7.5 lpm_10nm
Right_Lung_9 lpm_10nm
Left_Lung_9 lpm_10nm
Right_Lung_25 lpm_10nm
Left_lung_25 lpm_10nm
(c)
Particle Position (m)
-0.05
-0.1
-0.15
-0.2
-0.25
Particle Deposition Density
Right_Lung_7.5 lpm_50nm
Left_Lung_7.5 lpm_50nm
Right_Lung_9 lpm_50nm
Left_Lung_9 lpm_50nm
Right_Lung_25 lpm_50nm
Left_lung_25 lpm_50nm
(d)
Particle Position (m)
-0.05
-0.1
-0.15
-0.2
-0.25
Particle Depition Density
Right_Lung_7.5 lpm_1000nm
Left_Lung_7.5 lpm_1000nm
Right_Lung_9 lpm_1000nm
Left_Lung_9 lpm_1000nm
Right_Lung_25 lpm_1000nm
Left_lung_25 lpm_1000nm

Fig. 6

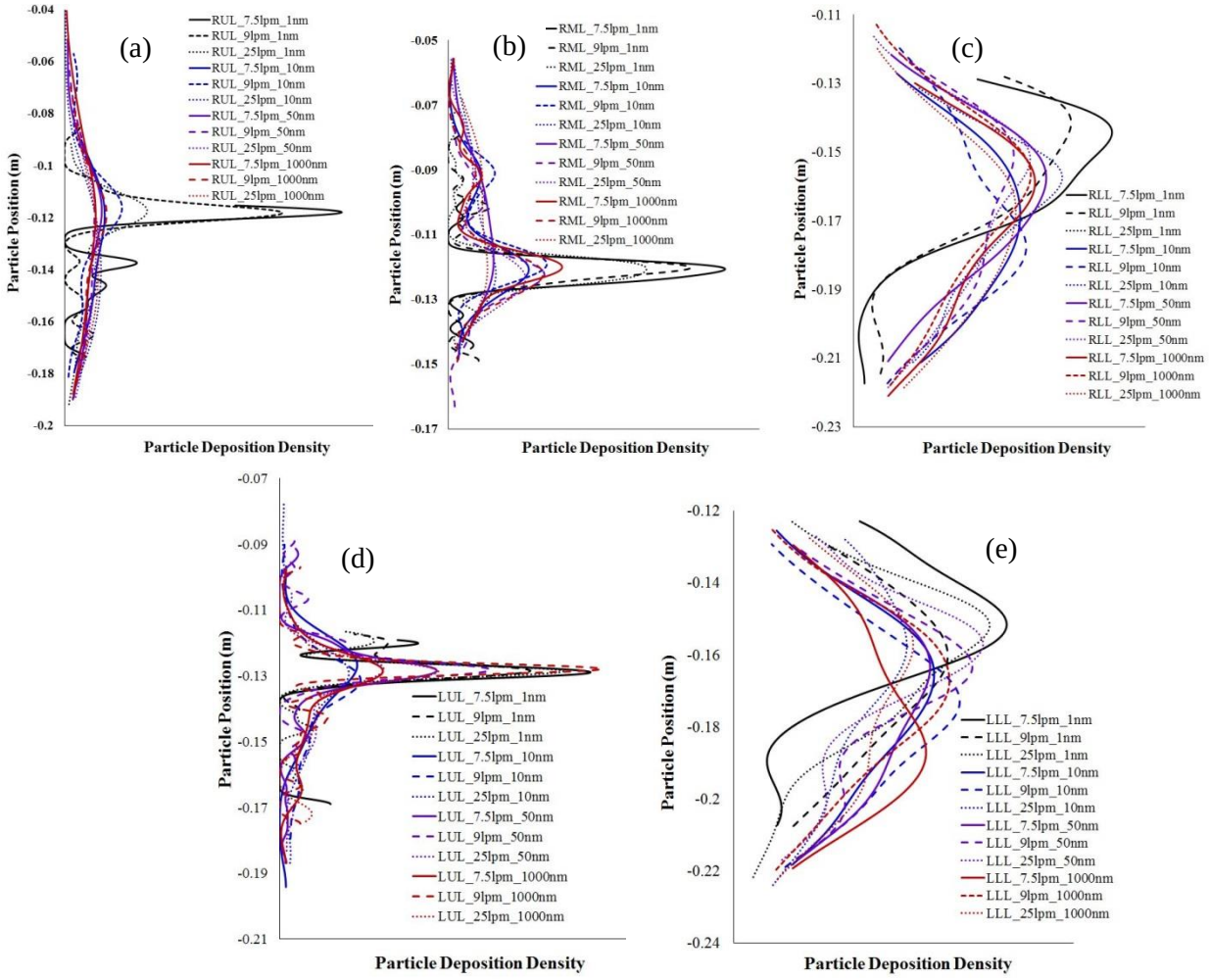
(a)
Particle Position (m)
Particle Deposition Density
RUL_7.5lpm_1nm
RUL_9lpm_1nm
RUL_25lpm_1nm
RUL_7.5lpm_10nm
RUL_9lpm_10nm
RUL_25lpm_10nm
RUL_7.5lpm_50nm
RUL_9lpm_50nm
RUL_25lpm_50nm
RUL_7.5lpm_1000nm
RUL_9lpm_1000nm
RUL_25lpm_1000nm
(b)
Particle Position (m)
Particle Deposition Density
RML_7.5lpm_1nm
RML_9lpm_1nm
RML_25lpm_1nm
RML_7.5lpm_10nm
RML_9lpm_10nm
RML_25lpm_10nm
RML_7.5lpm_50nm
RML_9lpm_50nm
RML_25lpm_50nm
RML_7.5lpm_1000nm
RML_9lpm_1000nm
RML_25lpm_1000nm
(c)
Particle Position (m)
Particle Deposition Density
RLL_7.5lpm_1nm
RLL_9lpm_1nm
RLL_25lpm_1nm
RLL_7.5lpm_10nm
RLL_9lpm_10nm
RLL_25lpm_10nm
RLL_7.5lpm_50nm
RLL_9lpm_50nm
RLL_25lpm_50nm
RLL_7.5lpm_1000nm
RLL_9lpm_1000nm
RLL_25lpm_1000nm
(d)
Particle Position (m)
Particle Deposition Density
LUL_7.5lpm_1nm
LUL_9lpm_1nm
LUL_25lpm_1nm
LUL_7.5lpm_10nm
LUL_9lpm_10nm
LUL_25lpm_10nm
LUL_7.5lpm_50nm
LUL_9lpm_50nm
LUL_25lpm_50nm
LUL_7.5lpm_1000nm
LUL_9lpm_1000nm
LUL_25lpm_1000nm
(e)
Particle Position (m)
Particle Deposition Density
LLL_7.5lpm_1nm
LLL_9lpm_1nm
LLL_25lpm_1nm
LLL_7.5lpm_10nm
LLL_9lpm_10nm
LLL_25lpm_10nm
LLL_7.5lpm_50nm
LLL_9lpm_50nm
LLL_25lpm_50nm
LLL_7.5lpm_1000nm
LLL_9lpm_1000nm
LLL_25lpm_1000nm

Fig. 7

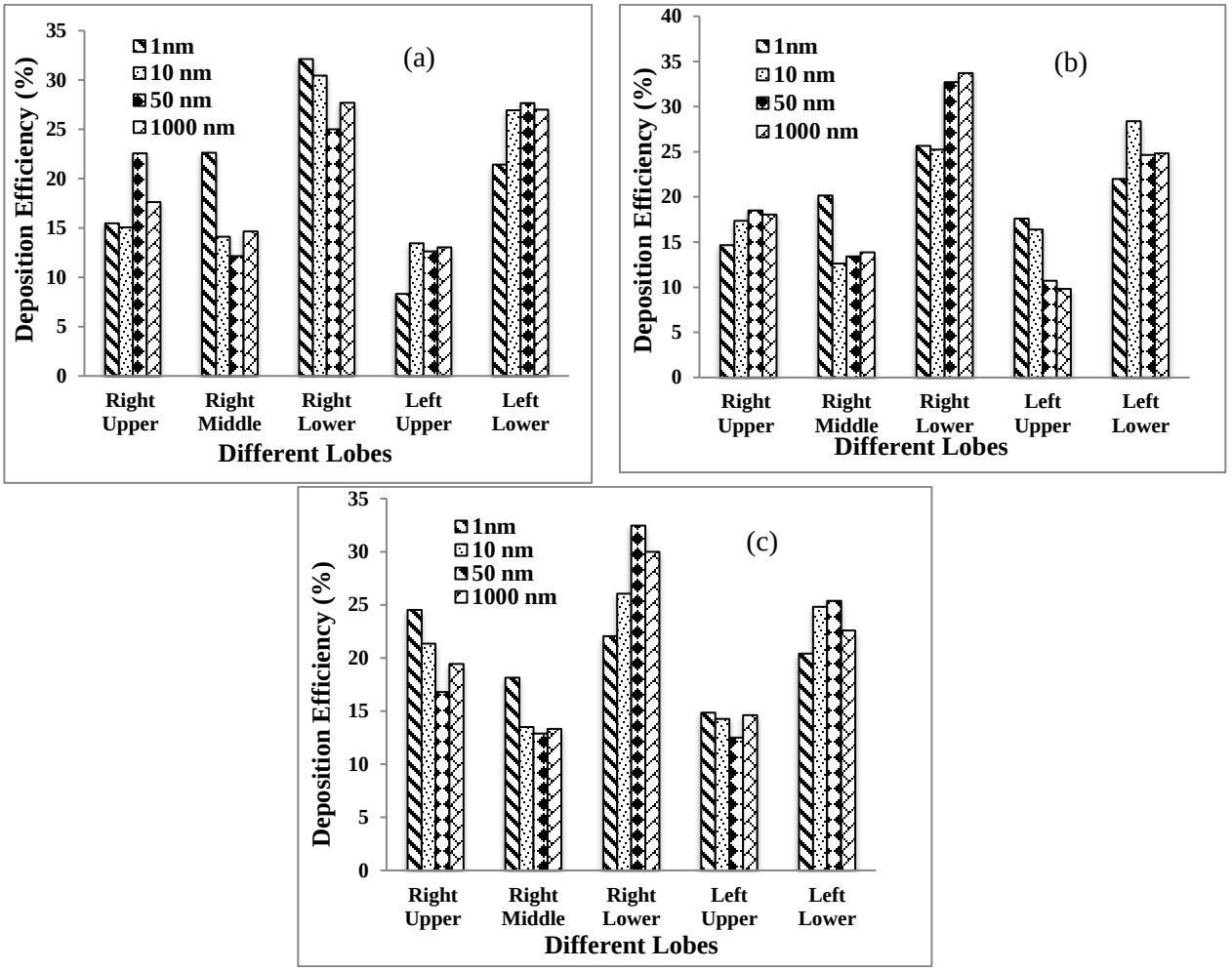
(a)
1nm
10 nm
50 nm
1000 nm
Deposition Efficiency (%)
0
5
10
15
20
25
30
35
Right Upper
Right Middle
Right Lower
Left Upper
Left Lower
Different Lobes
(b)
1nm
10 nm
50 nm
1000 nm
Deposition Efficiency (%)
0
5
10
15
20
25
30
35
40
Right Upper
Right Middle
Right Lower
Left Upper
Left Lower
Different Lobes
(c)
1nm
10 nm
50 nm
1000 nm
Deposition Efficiency (%)
0
5
10
15
20
25
30
35
Right Upper
Right Middle
Right Lower
Left Upper
Left Lower
Different Lobes

Fig. 8

Appendix Figures

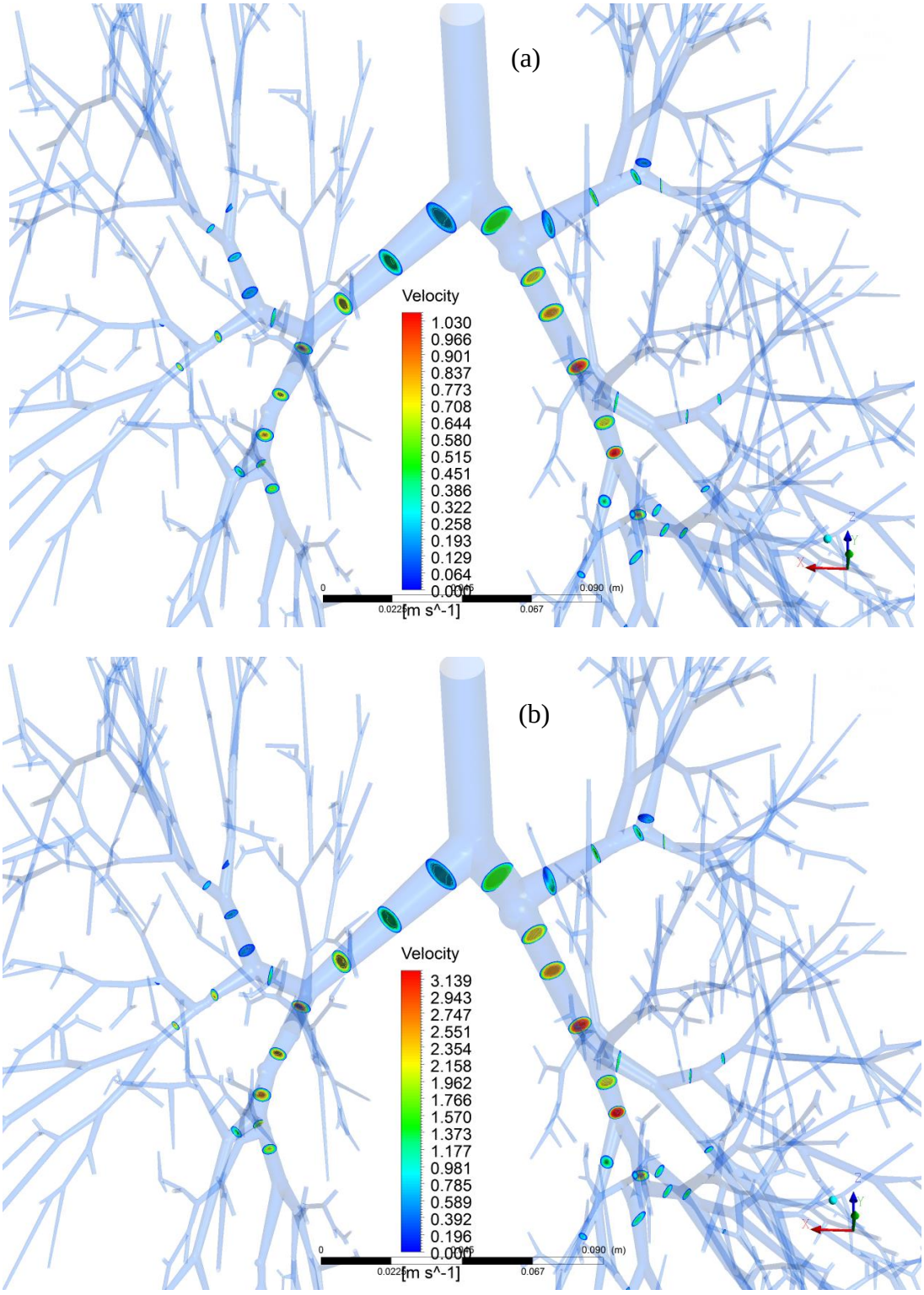

Fig. A1

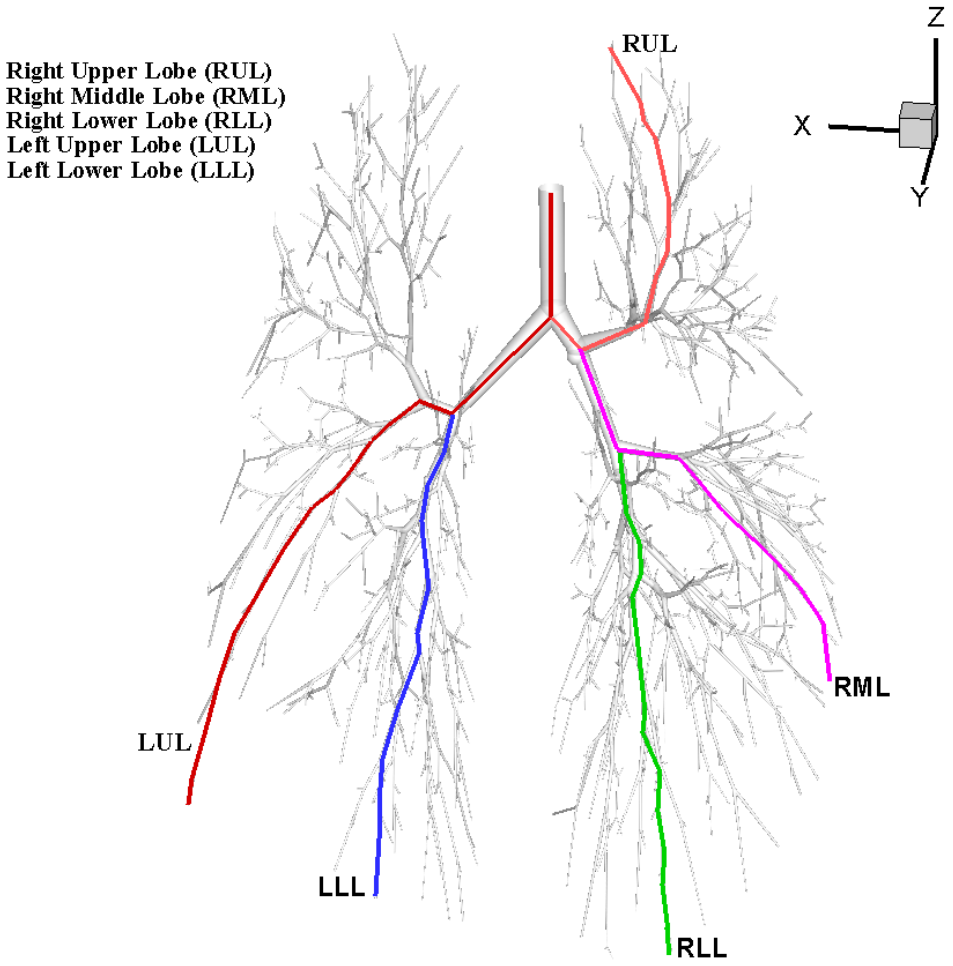
Right Upper Lobe (RUL)
Right Middle Lobe (RML)
Right Lower Lobe (RLL)
Left Upper Lobe (LUL)
Left Lower Lobe (LLL)
RUL
Z
X
Y
RML
LUL
LLL
RLL

Fig. A2